

Nano-Derived CuO Micro-Chemical Sensors
for Explosives Detection

Yamila Mariel Omar
directed by Dr. Edward Sabolsky
and Dr. Celso Aldao

West Virginia University, WV, USA
Universidad Nacional de Mar del Plata, BA, Argentina

July, 2012



RINFI se desarrolla en forma conjunta entre el INTEMA y la Biblioteca de la Facultad de Ingeniería de la Universidad Nacional de Mar del Plata.

Tiene como objetivo recopilar, organizar, gestionar, difundir y preservar documentos digitales en Ingeniería, Ciencia y Tecnología de Materiales y Ciencias Afines.

A través del Acceso Abierto, se pretende aumentar la visibilidad y el impacto de los resultados de la investigación, asumiendo las políticas y cumpliendo con los protocolos y estándares internacionales para la interoperabilidad entre repositorios



Esta obra está bajo una [Licencia Creative Commons Atribución-
NoComercial-CompartirIgual 4.0 Internacional](https://creativecommons.org/licenses/by-nc-sa/4.0/).

Abstract

Remote detection of explosive materials has become a priority to ensure airport safety. Explosives are easily hidden in luggage, mail, vehicles, aircraft as well as on people, and contain less and less metal parts making their detection by means of metal detectors highly unreliable. Although there are some analytical techniques available to detect explosives, they involve bulky equipment and take long time to report their results. For this reason, highly sensitive, portable chemical sensors showing fast response to explosive analytes or their fingerprint gases are being developed as an alternative. In the present work, metal-oxide sensors containing cupric oxide as sensing material on top of platinum interdigitated electrodes were constructed onto alumina substrates. The sensing material was obtained following two different processing routes: thermal oxidation of sputtered copper metal and hydrothermal growth from a water solution of copper nitrate, obtaining different morphologies. Sensors were dynamically tested in order to detect hydrogen gas in humid air between room temperature and 400°C. Sensors showed responses at testing temperatures as low as 200°C. Results indicated that sensing materials with grain sizes close to the space-charge region width have higher sensitivity to the presence of hydrogen gas and show faster response. The sensing mechanism in terms of inter-granular potential barriers was explained as an alternative to the sensing mechanisms found in the literature.

Acknowledgements

I would like to start by thanking Dr. Edward Sabolsky for giving me the greatest opportunity in my life. This was an experience I will never forget since it helped me realize that through passion and hard work comes amazing results.

I also want to thank Dr. Ever Barbero. Without his support, I would have never survived the US.

I would like to give special thanks to Dr. Kolin Brown, Dr. Weiqiang Ding and Mr. Harley Hart from the Shared Research Facilities at WVU. They trained me on every piece of equipment I needed and had the patience required to explain me how to use the facilities over and over. Without them, all this would have been impossible.

I want to thank all the awesome people in Dr. Sabolky's team: Christina Yarborough, Tim Weadon, Engin Ciftyurek, Nacho Muchenik, Josh Mullenax, Sodith Gandavarapu, Borja Cantero, Phil Gansor, Victor Sivaneri, Jonathan Yancey, Sheldon Blackshire, Charles Ndhlovu and Kathy Sabolsky. Thank you all for the good times in and out of the lab!

A very special thank you to Dr. Celso Aldao. He accepted the challenge of helping me understand the physics behind my experiments. Thank you for all the meetings and for going into the trouble of reading my Final Project again and again until it was perfect!

Special thanks to Fundación Roberto Rocca. Without their support I would probably not be here today.

And last but not least, thank you Mom! You encouraged me to reach my potential. This Final Project is dedicated to you.

Contents

1	Introduction	1
1.1	Prologue	1
1.2	Literature Review	1
1.2.1	Introduction to Metal-Oxide Semiconductor Chemi-Resistive Sensors	1
1.2.2	Advantages and Disadvantages of Metal Oxide Semiconductor (MOS) Sensing Materials	5
1.2.3	Copper oxides: Cu ₂ O and CuO as Sensing Materials	6
1.3	Problem Overview	7
2	Experimental	8
2.1	Substrates Fabrication	8
2.1.1	Alumina Slurry	8
2.1.2	Substrates Fabrication	8
2.1.3	Substrates Cleaning	9
2.2	Interdigitated Electrodes (IDEs) Fabrication	9
2.2.1	Photolithography	9
2.2.2	Sputtering	10
2.2.3	Lift-off procedure	10
2.3	CuO Sensing Nano-Powder Fabrication	10
2.3.1	Seeding	10
2.3.2	Route 1: Thermal Oxidation	11
2.3.3	Route 2: Hydrothermal Process	12
2.4	Characterization of CuO	13
2.5	Testing procedure	13
3	Results: Route 1, Thermal Oxidation	14
3.1	Test Results	14
3.2	Alternative Explanation for the Sensing Mechanism in Terms of Intergranular Potential Barriers	21
3.3	Characterization of CuO	22
3.3.1	X-Ray Diffraction	22
3.3.2	Scanning Electron Microscopy	22

4	Results: Route 2, Hydrothermal Process	25
4.1	Test Results	25
4.2	Sensing Mechanism in Terms of Intergranular Potential Barriers	28
4.2.1	Gas Sensing Mechanism and the Role of Surface Reactions	28
4.2.2	Effect of Particle Size on Sensitivity	29
4.3	Characterization of the nano-crystals obtained by the hydrothermal process	29
4.3.1	X-Ray Diffraction	29
4.3.2	Scanning Electron Microscopy	30
5	Conclusions	32
5.1	Future Work	33
A	Deposition Rate Studies	34
A.1	Pt Deposition Rate Study	34
A.2	Cu Deposition Rate Study	34
B	Inter-Digitated Electrodes Dimensions	36
	Bibliography	37

Chapter 1

Introduction

1.1 Prologue

Recently, the early detection of explosive materials hidden in luggage, mail, vehicles, aircraft, as well as on people, has become a priority in airports' security [1]. In the past, explosives were easily detected by means of metal detectors. However, nowadays, explosives contain less and less metal parts, or are even completely plastic, making this detection technique increasingly unreliable [2].

At present, trained canines are being used successfully for this task [3]. However, remote or automated detection is preferable since these devices do not need to get into contact with the item being checked and they enable definite identification of the explosive that has been detected [4]. Some analytical techniques, such as gas chromatography coupled to a mass spectrometer, neutron activation analysis, and electron capture detection are employed to recognize specific explosives or their signal vapors [5] [6]. Although these techniques are highly selective, they are cumbersome and not easily fielded in a small, low power package, and take a long time to report analytical results [2].

Therefore, the development of more compact, low-cost and efficient instruments with short time response is highly desired for facilitating the task of on-site detection of explosives. An electronic nose (eNose) would be able to mimic and even exceed dogs advantages in this task without the drawbacks, since they also have the potential to accurately determine the composition of the explosive in question, they can be fielded in small pieces of equipment easily handled and they would imply low electrical consumption. However, to reach these goals extensive testing and the development of a neural network to analyze experimental data are needed.

1.2 Literature Review

1.2.1 Introduction to Metal-Oxide Semiconductor Chemi-Resistive Sensors

An electronic nose is usually composed of a chemical sensing system and a pattern-recognition system such as an artificial neural network. The chemical gas sensing system can be made of metal-oxide semiconductors (MOS). This kind of sensors show great sensitivity, low-cost and are easy to manufacture [7] [8] [9].

These gas sensors require an insulating substrate where a conductive electrode is deposited. Alumina, Al_2O_3 , is often the substrate of choice due to its high electrical resistance, thermal stability and the ability of many metal oxides to adhere effectively to it [10]. Electrodes are usually made of highly conductive noble metals such as platinum, gold or silver. The metal used depends on the working temperatures of the device. The semiconductor sensing material is deposited on top of the planarized substrate as shown in Figure 1.1.

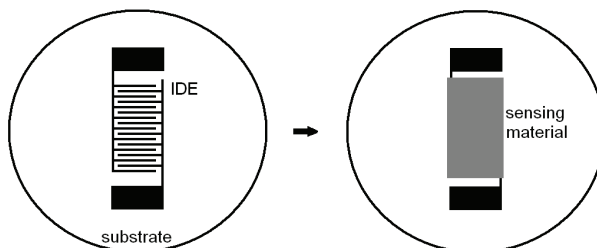


Figure 1.1: Schematics of a micro-chemical sensor

In recent works [11] [12] [13], the semiconductor metal-oxide sensing materials are in the nano-scale showing different morphologies such as wires, rods, spheres, cubes, etc. The goal is to present an ultra-high surface area for gas interaction, as well as, to present non-equilibrium surfaces for enhanced gas adsorption.

In Duc Hoa et al. work [12], CuO chemical sensors, in which the sensing material was obtained by thermal oxidation of sputtered Cu at different temperatures ranging from 300°C to 800°C , were tested. Fig. 1.2 is a reproduction of Duc Hoa's work showing the greatest sensitivity ($S = R/R_0$) for an oxidation temperature of 400°C . In this paper, the authors conclude that the grain size (or surface area), the porosity and the density of Cu vacancies in the material are the parameters that affect the response to the analyte, the last one being the dominant one. If this were the case, the concentration of Cu vacancies would be the highest at 400°C . However, the stoichiometry analysis carried out via XPS does not support their hypothesis. Finally, they conclude that the change in response in CuO thin films was mainly caused by the combined effect of the grain size and porosity and that details regarding Cu vacancies should be further explored.

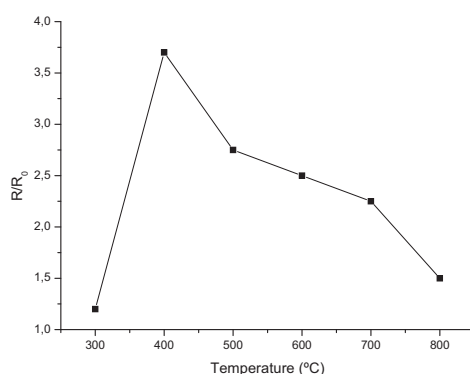


Figure 1.2: Maximum sensitivity upon exposure to 6% H_2 gas in air at 250°C vs. oxidation temperature reproduced from Ref. [12]. It is shown that the highest sensitivity is obtained in samples oxidized at 400°C .

Fig. 1.3 reproduces the SEM characterization in the mentioned work showing an increase in grain size, and therefore, a decrease in surface area, with thermal oxidation temperature. This data in combination with results in Fig. 1.2, shows a correlation between surface area and sensitivity. As it was expected, the lower bonding temperature resulted in a finer grain size or higher surface area absorber. Then, it can be concluded that higher surface areas obtained by oxidizing at lower temperatures result in higher sensitivities.

In Fig. 1.2, the sensitivity of the samples oxidized at 300°C is reported to be the lowest. This is because Cu thin films oxidize only partially at this temperature giving a mixture of Cu and Cu₂O, as it is supported by XRD results [14]. XRD results also show that Cu₂O is the main oxidation product with a small amount of CuO after the oxidation at 400 and 500°C. For temperatures higher than 600°C, only CuO is formed. This will be further discussed in subsection 1.2.3.

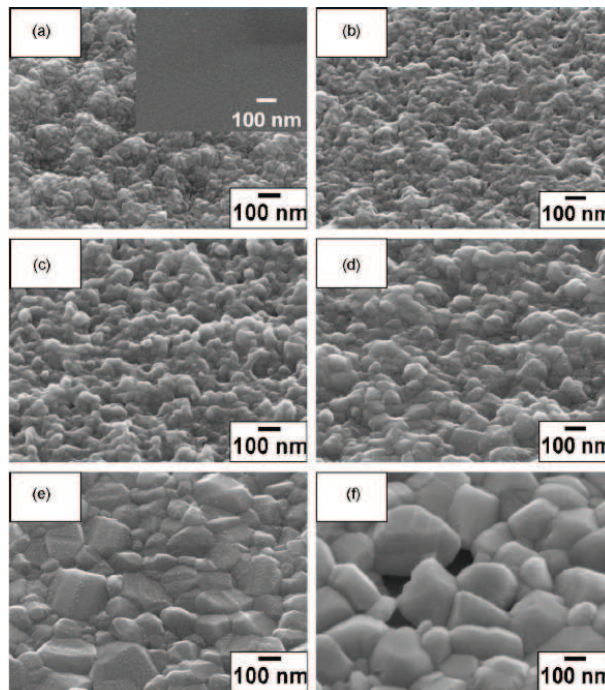
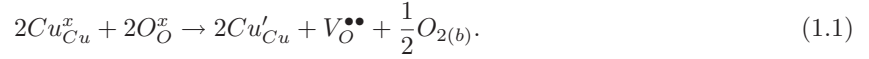


Figure 1.3: SEM characterization reproduced from Ref. [12] (a)300, (b)400, (c)500, (d)600, (e)700 and (f)800°C thermal oxidation temperatures. Thermal oxidation time: 30 minutes. Insert in a) shows the surface of the Cu seeds.

A previously mentioned variable, Cu vacancies in CuO, have to be taken into account to explain the sensing mechanism. An increase in Cu vacancies can be attained by quenching a high temperature state, since the number of defects in an oxide increases with increasing temperature. This would be reflected in the oxide electrical properties. But how are these vacancies created? One possible mechanism requires a change in Cu valence as stated in $Cu^{+2} + e^- \leftrightarrow Cu^{+1}$.

It has been long known that hydrogen sensing implies its reaction with oxygen as stated in $H_2 + \frac{1}{2}O_2 \leftrightarrow H_2O$. If the oxygen precedence is the bulk of the CuO crystal, then a change in Cu valence would occur as shown in Eq. 1.1,



Oxygen from the bulk of the crystal diffuses to the surface and reacts with the analyte, hydrogen gas (see Eq. 1.2). Oxygen vacancies are created as stated in Eq. 1.1. Each oxygen vacancy has positive charge +2. At the same time, Cu vacancies are also created given Cu^{+2} is reduced to Cu^{+1} as a result of hydrogen reducing power. Then, Cu^{+1} atoms occupy Cu^{+2} sites in the crystal lattice producing a negative charge each. This increase in Cu^{+1} atoms occupying Cu^{+2} sites in the lattice leads to an increase in resistivity. This phenomenon is supported by resistivity values of CuO and Cu_2O since it is known that cuprous oxide has high resistivity, ranging from 10^2 - $10^6 \Omega \cdot cm$ depending on the method of preparation [15], while cupric oxide has lower resistivity values ranging from $10^{-2} - 10 \Omega \cdot cm$ [16]. Furthermore, the formation of stable Cu_2O from reduction of CuO nano-particles in the presence of a reducing agent is supported in the literature [17].

Explosives, even common ones, are usually formed by complex molecules. For example, the molecules of picric acid also known as 2,4,6-trinitrophenol, 2,6 dinitrotoluene and trinitrotoluene are shown in Figure 1.4. These complex molecules react with oxygen gas during the combustion reaction giving simpler gases as products. These simpler gases are usually a mixture of H_2 , N_2 , NO_x , CO_x and H_2O and are known as “fingerprint gases”. The combination and the amount of each gas present after combustion are unique for each explosive, making it possible to differentiate them by means of an artificial neural network.

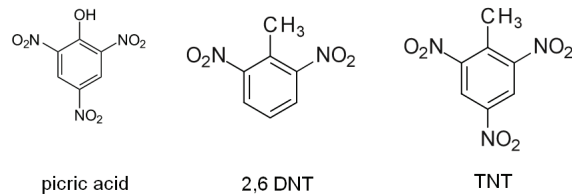


Figure 1.4: Common explosives complex molecules

When some of these fingerprint gases are in contact with the sensing materials on chemical sensors, they are adsorbed to the surface and the electrical properties of the sensor change, such as the resistance R . This can be measured as an electric signal.

A second sensing mechanism found in current literature of metal-oxide sensors considers that the reaction takes place in the surface of the sensing material. This surface reaction is complex and therefore, it is the subject of discussion in several papers [18] [19] [20]. In the case of hydrogen sensors, for example, the change in metal-oxide resistance results from a gain in surface electrons following reaction of hydrogen with adsorbed oxygen. The surface reactions involve two steps. Firstly, oxygen chemisorbs on the metal-oxide surface as shown in Eq. 1.3



This decreases the surface conductivity in the case of n-type semiconductors, since the carriers, electrons, are being used to charge oxygen at the surface. On the other hand, p-type semiconductors conductivity is increased given that more “electron holes” are created.

Subsequently, hydrogen adsorbs and reacts with the adsorbed oxygen in a reaction expressed simply by Eq. 1.4



For n-type semiconducting oxides, e.g. SnO_2 , electrons are donated into the conduction band. As a result, the resistance of this type of oxide decreases in the presence of hydrogen and the magnitude of the resistance change can be related to the hydrogen concentration [10]. In contrast, in the case of p-type semiconducting oxides, such as CuO , where the majority of the carriers are holes, the resistance is increased by the presence of hydrogen since the donated electrons recombine with the holes in the conduction band diminishing the overall conductivity [12] as shown in Eq. 1.5,



In Fig. 1.5, schematics of the expected response for p-type and n-type semiconductors sensing materials are shown.

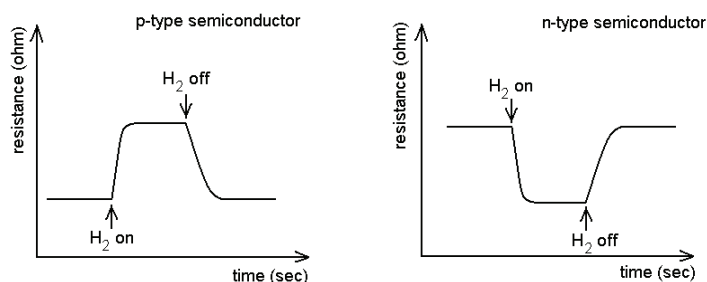


Figure 1.5: Typical response to hydrogen gas for p- and n-type semiconductors

However, the explanation presented in the previous paragraphs corresponds to bulk conductivity rather than a surface reaction as the process is claimed to be. Therefore, it is the goal of the present work to explain the experimental results from this project, as well as those encountered in literature, by means of a surface phenomenon such as intergranular potential barriers. This will be further developed in Chapters 3 and 4.

1.2.2 Advantages and Disadvantages of Metal Oxide Semiconductor (MOS) Sensing Materials

The advantages and disadvantages of MOS sensing materials are thoroughly described in Hübner’s review [10].

Some of the advantages are

- They have high sensitivity and fast response, which makes them appropriate for the detection of low concentrations of gases.

- They can operate in a wide range of temperatures, from cryogenic temperatures (like hydrazine sensors for spacial applications) to moderately high temperatures (like hydrogen sensors for industrial applications, 500-600°C).
- Their lifetime is acceptable and their manufacture is low cost.
- The power consumption they require to function is modest.

Among the disadvantages,

- Chemi-resistive sensors have poor selectivity. This means that their response changes in the presence of certain gases as CO_x , NO_x , H_2S and humidity, not only H_2 .
- They usually cannot operate at high temperatures ($> 600^\circ\text{C}$). This is due to the poor stability of nano-scale materials at high temperatures, i.e. the sensing material coarsens when exposed to temperatures higher than half of the homologous temperature leading to a decrease in surface area which leads to a decrease in sensitivity.
- They are susceptible to aging and memory effects.
- They usually require O_2 to function.

1.2.3 Copper oxides: Cu_2O and CuO as Sensing Materials

Cuprous oxide is a p-type semiconductor with unique optical and magnetic properties. It has potential applications in solar energy conversion, electronics, magnetic storage, catalysis and gas sensors. Cupric oxide is also a potential material with many applications in catalysis, gas sensing and lithium-copper oxide electrochemical cells. CuO was, in fact, the first kind of humidity sensing material found by Braver et al. in 1931 [21].

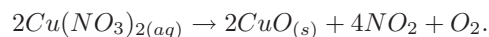
In view of such utilizations, intense efforts have been devoted to the development of many kinds of morphologies, such as wires, cubes, spheres, cages, whiskers and so forth [21] [22]. In fact, organized nano-structured materials feature unique properties and attractive performances thanks to their large surface-to-volume ratio, the presence of size effects and of various defects, often resulting in an unexpected reactivity [23] [24]. In the field of gas sensing, the combined influence of the above phenomena is significantly advantageous in order to achieve high gas sensitivity and a rapid response [25].

In this context, Cu_xO ($x=1,2$) nano-systems have received an increasing attention for various applications in solid state gas sensors. Cu_xO and Cu_xO composites (CuO-SnO_2 , CuO-ZnO , etc) has been found to be sensitive to H_2 [10], CO_x [24], NO_x [26], H_2S [27], and moisture [13].

Copper oxides can be obtained following several routes. Thermal oxidation, also known as thermal annealing, is an attractive method to obtain copper oxides from Cu thin films due to its simplicity [28]. This process is also convenient and fast, and permits the synthesis of nanostructures such as nanowires [14].

As described in previous subsections, Cu_2O is the main oxide formed at low oxidation temperatures, below 500°C . However, traces of CuO have been reported in samples oxidized at 400°C [29]. At temperatures above 500°C , CuO is obtained.

Copper oxides can also be obtained by a hydrothermal process. This method requires an aqueous solution of a copper oxide precursor, such as copper nitrate, and an autoclave. Nanoscale crystals with high surface area can be obtained by this route as described by the following chemical Eq.



There are other routes to obtain copper oxides, such as vapor-liquid-solid growth, epitaxial growth, vapor-solid growth, wet chemical methods and electrospinning. These techniques will not be further discussed in the present work.

1.3 Problem Overview

This research expanded on previous studies of hydrogen gas sensors and aims to create environmentally inert prototypes, with low power requirements and able to be configured in micro-arrays for strategic placement in explosive detectors.

A schematic of the target gas sensor was previously illustrated in Fig. 1.1. The sensors consist of an alumina substrate, a metallic interdigitized electrode (IDE) and a copper oxide semiconductor that serves as the sensing material on the outermost layer.

Two experimental tracks were investigated for the fabrication of micro-sensors of a maximum length of 5000 μm . This involved techniques as photolithography, sputtering and thermal oxidation or hydrothermal growth of nano-crystals. Variables of interest in this study are described in detail in the experimental section.

Testing of the micro-chemical sensors was conducted at temperatures ranging from room temperature to 400°C to prove if the sensors are capable of sensing fingerprint gases such as hydrogen. Further testing involving other fingerprint gases such as CO_x and NO_x needs to be conducted to determine if the sensing material presents changes in resistance in their presence.

Chapter 2

Experimental

2.1 Substrates Fabrication

2.1.1 Alumina Slurry

Alumina slurry is prepared to make alumina tape by tape casting. The composition used is that of Table 2.1, where PI, PII and PBV are binders.

Component	Amount (g)
Al ₂ O ₃	60
Solvent	38.68
FO Oil	1.40
P I	3
P II	3
PBV	6

Table 2.1: Solution Contents

The alumina powder is mixed with the fish oil and a solvent made by a mixture of 50 wt% of xylene and 50 wt% of ethanol. The mixture is milled for 4 hours. Then, the PI, PII and PVB are added. The new mixture is milled for 12 hours and then tape casted.

2.1.2 Substrates Fabrication

Alumina tape fabricated by tape casting is cut into smaller pieces and stuck in order to obtain a 400 μm thick piece. This is laminated at 100°C at pressures of 70 psi and 70 kpsi for a total of 30 minutes. Then, the alumina tape is cut using a laser cutter into circular substrates with holes, which will be used in the future to attach wires, as shown in Figure 2.1. The substrates are placed in an oven with a heating rate of 1°C/min up to 600°C to burn the polymeric binder. After this, they are taken up to 1500°C to sinterize the alumina powder, followed by 6 hours of forging at 1500°C. The final diameter of the substrates is of 1.5 cm and that of the holes of 100 μm . Then, the substrates are polished with several grades of diamond disks (from 600 to 1800) and diamond paste (from 7 μm to 0.5 μm). Finally, they are fired in a furnace at 800°C to burn any contaminant.

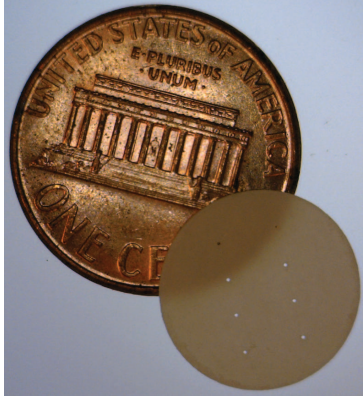


Figure 2.1: Alumina substrate with holes

2.1.3 Substrates Cleaning

The alumina substrates are cleaned in WVU Nano Shared Facilities' Cleanroom. The cleaning procedure involves a 10 minutes wash with acetone followed by a 10 minutes wash with methanol. The substrates are then washed with de-ionized water and dried with nitrogen gas. Finally, they are placed on a hot-plate for 20 minutes at 120°C to evaporate any adsorbed moisture.

2.2 Interdigitated Electrodes (IDEs) Fabrication

2.2.1 Photolithography

The clean and polished Al_2O_3 substrates are coated with an approximate 1.5 μm layer of AZ5214E positive photoresist by spin coating using a Laurell Technologies 400 Series spin-coater. The two step program used is:

- 10 seconds at a velocity of 400 rpm and 330 rpm/sec acceleration,
- 15 seconds at a velocity of 3000 rpm and 440 rpm/sec acceleration.

The substrates are, then, soft-baked on a hot-plate for 5 minutes at 95°C. The coated substrates are exposed to UV light of 100 MJ/cm^2 energy through a soda-lime mask on a Suss Microtec MAG mask aligner. The intensity of the light is measured in MW/cm^2 before each exposure so the exposure time (in seconds) can be determined as follows:

$$time(sec) = \frac{UV \text{ light energy } (MJ/cm^2)}{intensity (MW/cm^2)} = \frac{100MJ/cm^2}{0.5MW/cm^2} = 200sec. \quad (2.1)$$

After exposure, the samples are developed by a quick immersion in AZ400K developer. The samples are washed with DI water and dried with nitrogen gas. The resulting pattern can be seen in Figure 2.2.



Figure 2.2: Pattern obtained after photolithography process (1.5x)

2.2.2 Sputtering

Following the patterning of the resist, a CVC 610 DC Magnetron sputter station is used next to deposit a thin titanium layer to ensure platinum adhesion to the substrates. This layer is necessary since the platinum and the alumina crystal structures are incompatible. Then, Pt was deposited under an argon plasma flow at 500 volts and 6.0 Torr for 9 minutes.

2.2.3 Lift-off procedure

The lift-off procedure is performed as follows: the substrates are immersed in an acetone bath for 10 minutes and periodically agitated with ultrasonication. This removes the polymer mold and any metal on its surface leaving only the interdigitated electrodes pattern. The samples are then placed in a methanol bath for 5 minutes, cleaned with deionized (DI) water and dried with nitrogen gas. The final result can be seen on Fig. 2.3. Dimensions of the Pt IDEs can be seen in Appendix B.

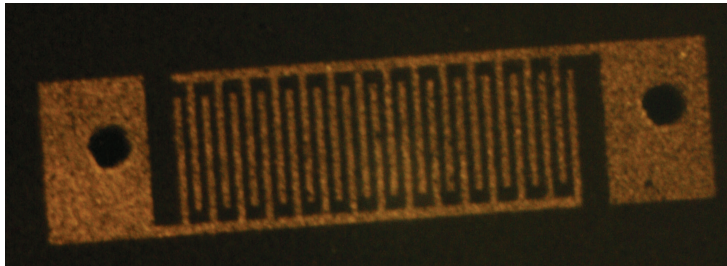


Figure 2.3: Pattern obtained after lift-off process (1.5x)

Fig. 2.4 summarizes the procedure used to fabricate the platinum electrodes.

2.3 CuO Sensing Nano-Powder Fabrication

2.3.1 Seeding

The Pt IDEs are seeded with Cu metal. This is accomplished by a multi-step procedure. First, the alumina substrates with fully developed IDEs are spin-coated with AZ5214E photoresist using the same spin rates explained in Section 2.2.1. After a soft-bake, the substrates are exposed to UV light under a negative soda-lime photomask in the Suss Microtec MAG mask aligner. The pads are aligned with the IDEs on

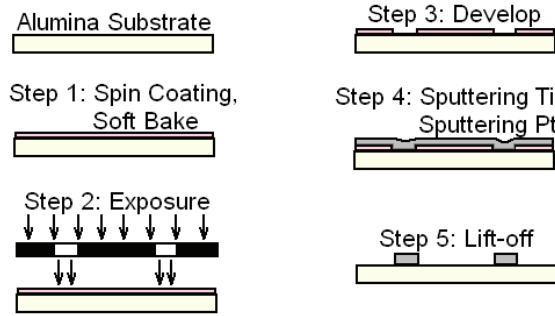


Figure 2.4: Summary of the procedure to create Pt IDEs

the substrates using a microscope. Next, the substrates are agitated in AZ400K developer during a quick immersion. This procedure creates a mold of rectangular pads over the IDE's fingers. The dimensions of these pads are proportional to the length of the IDE that they are matching.

The next step in the procedure is metal deposition via sputtering. The substrates are coated with a layer of copper (seeds) using the same sputtering station as for the Pt IDEs (see Subsection 2.2.2), with argon plasma flow at 490 V and 6.0 Torr for 8 minutes.

Finally, a lift-off procedure as explained in Subsection 2.2.3, is performed to reveal Cu pads on top of the Pt IDEs.

2.3.2 Route 1: Thermal Oxidation

Silver wires are attached to the $\text{Al}_2\text{O}_3/\text{Pt IDE}/\text{Cu}$ sensor using the holes previously cut with the laser cutter. To secure the wires, platinum ink is deposited onto the part of the wires laying on top of the Pt pads.

The whole device undergoes a thermal oxidation procedure in a tube furnace to oxidize the Cu into CuO , which will be the sensing material. A heating velocity of $5^\circ\text{C}/\text{min}$ up to 700°C is used. The samples are annealed at 700°C for 15 minutes in static air before being taken out of the furnace.

According to references [28] [29] [14], if the heating velocity is high enough, high surface-volume ratio CuO nanowires can be obtained.

Fig. 2.5 shows a picture of an undoped finished sensor ready to be tested.

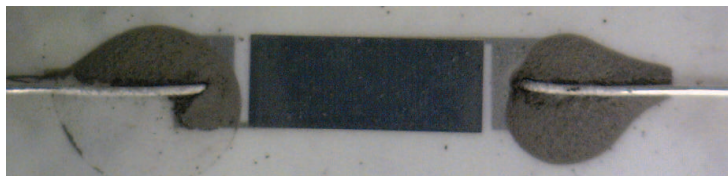


Figure 2.5: Finished undoped sensor

2.3.3 Route 2: Hydrothermal Process

A hydrothermal process would be an alternative to the thermal oxidation procedure to grow CuO nano-crystals. For this process, the layer of sputtered Cu was of ≈ 34 nm in thickness from a 30 sec sputtering time.

The alumina/IDE/Cu samples would undergo a templated hydrothermal process to grow $\text{Cu}_2\text{O}/\text{CuO}$ nano-platelets onto the Cu pads. This is accomplished by forming a highly basic solution ($\text{pH} > 11.1$) of copper nitrate hydrate ($\text{Cu}(\text{NO}_3)_2 \cdot x\text{H}_2\text{O}$) in de-ionized water via precipitation with ammonium hydroxide. The solution compositions used are outlined in Table 2.2.

Table 2.2: Solution contents

Run N°	Copper Nitrate Hydrate (g)	DI water (g)
1	1.25	125
2	1.25	80
3	1.69	80

The solution and alumina/IDE/Cu samples are held in a stainless steel autoclave at 100°C for 2 hours. After this, silver wires are attached to the IDEs using the holes and Pt ink to secure them. The sensor is taken to a furnace up to 400°C to burn the binder in the Pt ink.

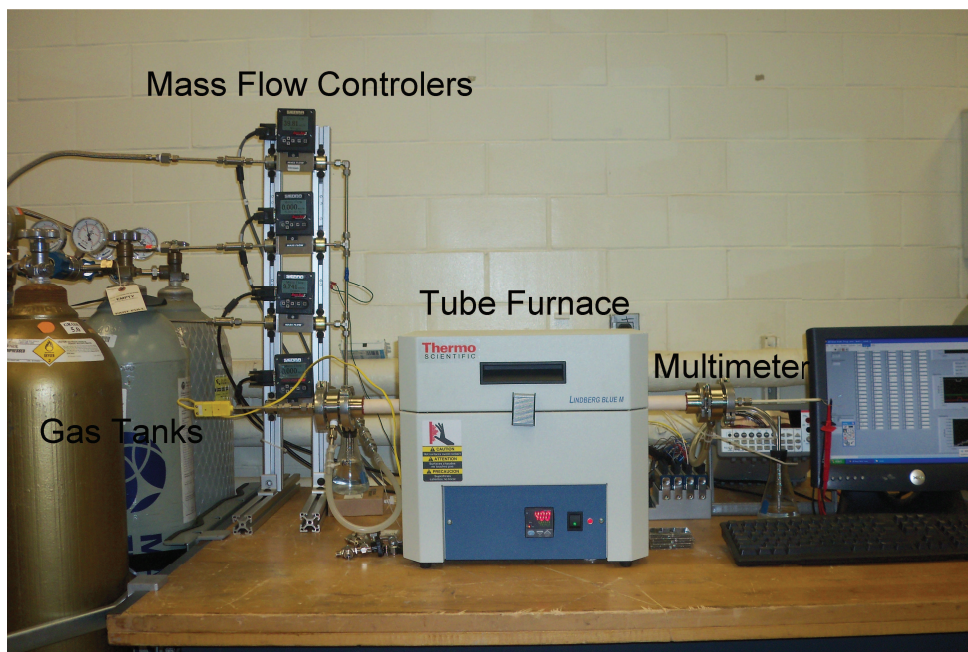


Figure 2.6: Test stand used to evaluate the sensors sensitivity to hydrogen gas

2.4 Characterization of CuO

The CuO obtained from either from thermal oxidation of Cu thin layers or hydrothermal growth of CuO nano-platelets is characterized using XRD to identify the phases that are present and by SEM to study the morphology of the sensing material. The XRD measurement are carried out using Cu K_{α} -X radiation of 8042.2 eV (Model: Bruker D8 Discovery).

2.5 Testing procedure

Testing of the sensor H_2 sensitivity is conducted in a $N_2/20\%O_2$ gas mixture. Fig. 2.6 displays the test stand used in this work. The test is completed at three different temperatures, ranging from room temperature to $400^{\circ}C$. Temperatures are measured by means of a thermocouple inside the tube of the tube furnace. For each temperature, the sensor is tested at different gas concentrations, ranging from 500 to 5000 ppm with different exposure times. The exact times are informed in detail in Table 2.3.

Table 2.3: Test times and concentrations.

H_2 Concentration (ppm)	time (min)	
0	40	Part 1
1000	10	
0	20	
2000	10	
0	20	
4000	10	
0	20	
2000	10	
0	20	
1000	10	
0	20	Part 2
1000	1	
0	20	
2000	1	
0	20	
4000	1	
0	20	
2000	1	
0	20	
1000	1	
0	25	Part 3
4000	0.5	
0	20	
4000	0.25	
0	20	
4000	0.08	

The test consists of three parts. In Part 1, sensors long time response is evaluated, while in Parts 2 and 3 sensors short time response are tested. Different gas concentrations at standard times of 1 minute are evaluated in Part 2, and high concentrations at really short times (30, 15 and 5 sec.) are tested in Part 3.

Chapter 3

Results: Route 1, Thermal Oxidation

3.1 Test Results

The sensors used for this chapter had ~ 280 nm thick Pt electrodes (5 min sputtering) and ~ 500 nm thick Cu seed layer (8 min sputtering) thermally oxidized at 700°C for 15 minutes. The sensor was tested at different temperatures ranging from room temperature to 400°C .

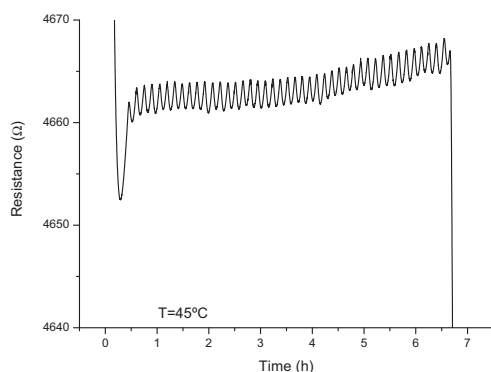


Figure 3.1: Test Results at 45°C

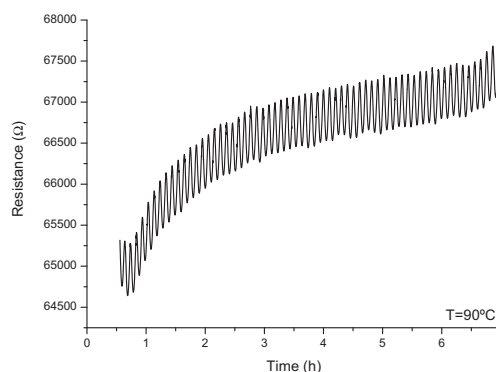


Figure 3.2: Test results at 90°C

In Figs. 3.1 and 3.2, the resistance measurements at 45 and 90°C are shown. The sensors did not show any response to hydrogen gas. The periodic oscillation of the reading is given by temperature fluctuations arising for the use of a poor temperature controller. Note that semiconductors suffer changes in conductivity (and therefore, resistivity) with temperature. At the testing temperatures, electrons are thermally excited to the “acceptor level” in a p-type semiconductor leading to carriers (holes) at the valence band. Fig. 3.3 shows the resistance behavior for a p-type semiconductor at different temperature ranges and the process by which enhanced conductivity is attained.

All semiconductors have infinite resistivity at 0K . Resistance starts dropping when the temperature is increased. Within the testing temperature range, resistance shows a slight increase. At these temperatures,

electrons from the valence band occupy all of the acceptor levels. If temperature is further increased, the Fermi Level reaches the middle of the band gap and the semiconductor becomes intrinsic which implies an increasing number of carriers with temperature.

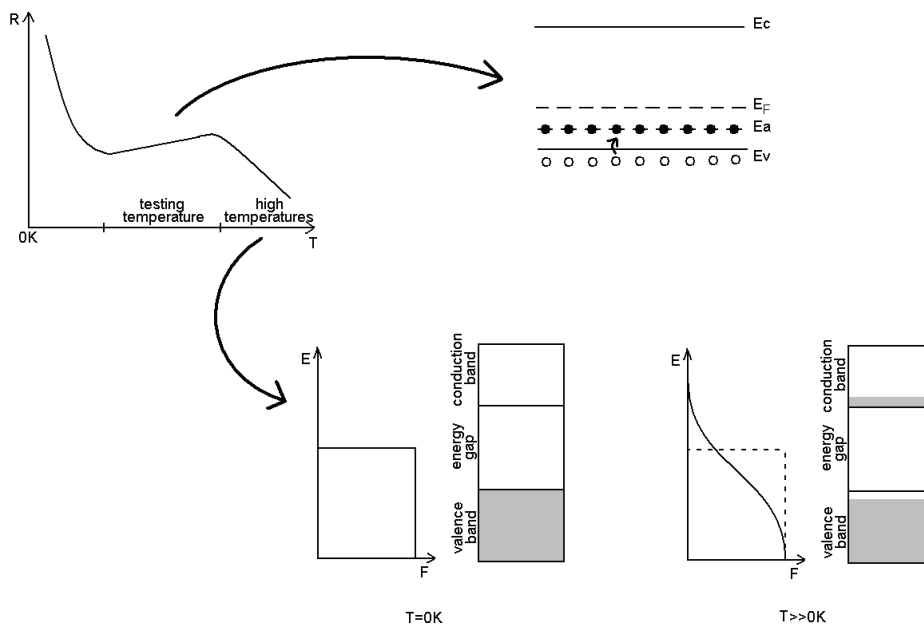


Figure 3.3: Fermi-Dirac Distribution

Those electrons excited to the acceptor level at test temperatures leave behind “electron holes”, i.e. unoccupied states in the valence band. The valence band electron holes are the main responsible for the semiconductor conductivity [30]. Therefore, by following what is stated in Fig. 3.3, a resistance increase is obtained when the temperature increases, and resistance drops when temperature decreases. However, in Figs. 3.1 and 3.2 the opposite happens. This can be observed in Fig. 3.4 where the temperature and resistance are plotted against time for a sensor tested at 45°C in humid air.

As it will be further explained in section 3.2, this behavior might indicate that holes overcome potential barriers at grain boundaries by jumping over them, and that this process is thermally activated.

The lack of response to the presence of hydrogen gas may be due to a process that does not take place at low temperatures. Possibly, the chemical reaction described in Eq. 1.4.

Results obtained while testing at 170°C (see Fig. 3.5) show a slight response to the presence of hydrogen gas. Nevertheless, this response is not acceptable for practical applications as the measurement is not stable with the resistance monotonously increasing during the test.

At 200°C (see Fig. 3.6), the sensor responds to hydrogen presence. However, there is noise in the measurement and the resistance is monotonously increasing during the extent of the test. The drift is of 108.1 Ω/h and indicates that the sensor is not stable. Probably, the interaction with the atmosphere involves huge time constants.

It can be seen that the increase in resistance is proportional to the hydrogen gas concentration, i.e. it

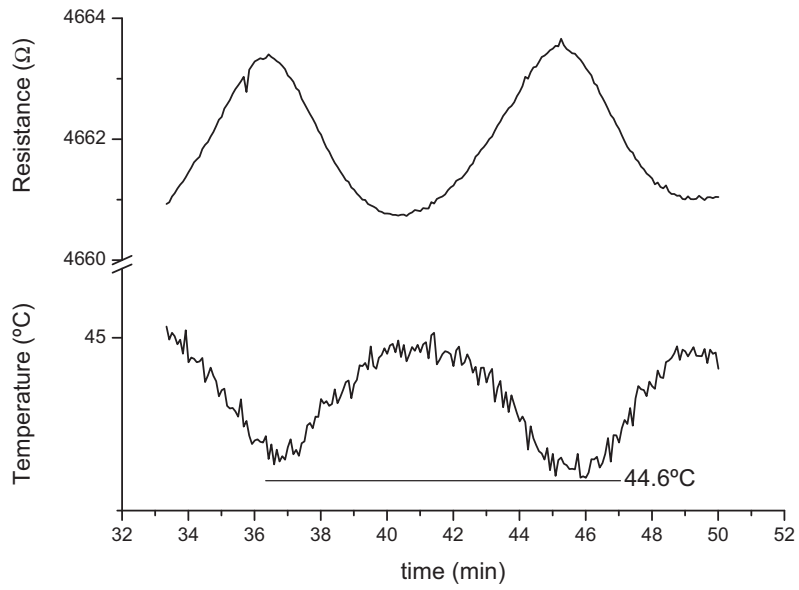


Figure 3.4: Temperature - Resistance analysis for a sensor tested at 45°C in a mixture of humid 80%N₂/20%O₂. Resistance peaks coincide with temperature valleys.

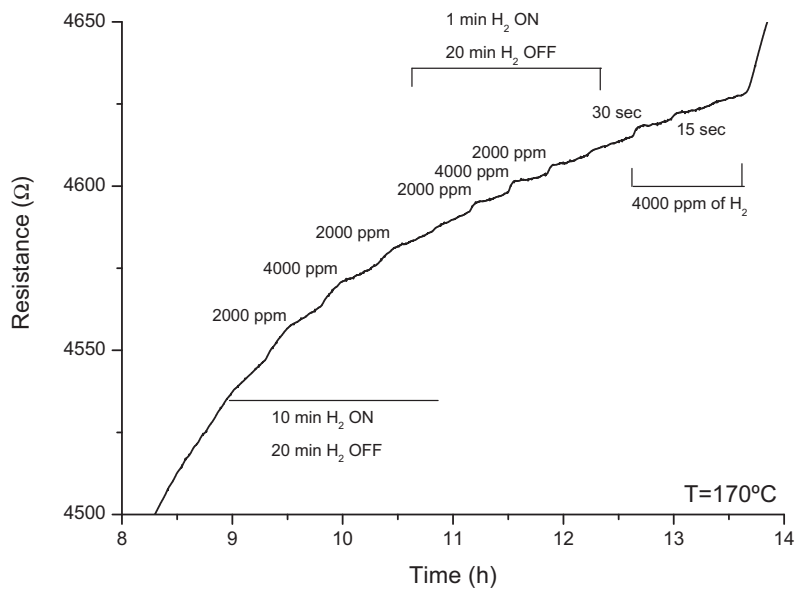


Figure 3.5: Test results at 170°C

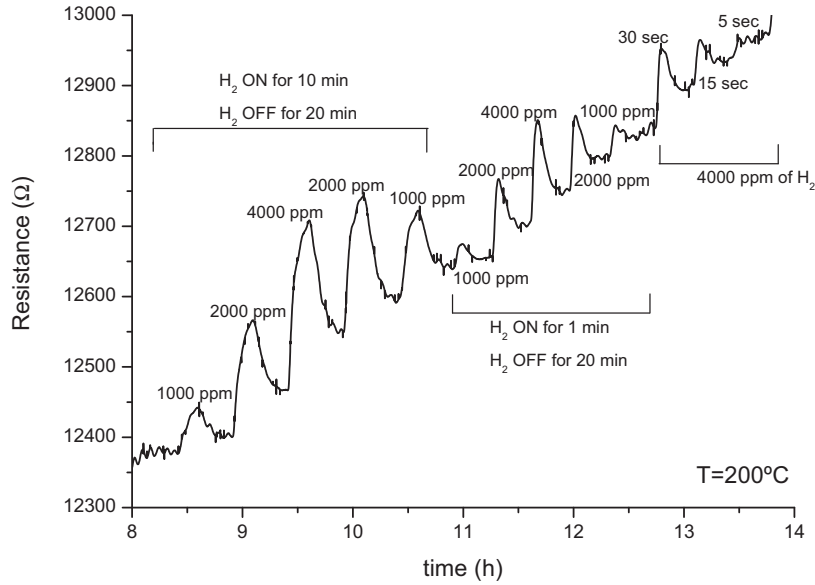


Figure 3.6: Test results at 200°C

is higher for higher concentrations of hydrogen gas. However, the resistance measurement is also dependent upon time of exposure, i.e., the change in resistance is higher for longer exposure times. For example, the absolute resistance change upon exposure to 4000 ppm of hydrogen gas for 10 minutes is $\approx 200\Omega$. However, when exposed to the same level of hydrogen gas but for 1 minute, the absolute resistance change is $\leq 150\Omega$.

Results obtained while testing sensors at temperatures $> 300^\circ\text{C}$ are shown in Figs. 3.8, 3.9 and 3.10. In all these cases, the drift was found to be $\approx 20\Omega/\text{h}$.

However, in current relevant literature about chemical sensors, the absolute resistance change is not the variable used to compare test results. Instead, the sensitivity S , defined as the ratio between the resistance measurement upon exposure to the test gas R and the resistance of the sensor in the reference gas R_g is used. Eq. 3.1 is the proper definition of the sensor response.

$$S = \frac{R}{R_g} \quad (3.1)$$

In Table 3.1, the sensitivity upon exposure to 4000 ppm of hydrogen gas for different times and temperatures is shown. This data can be easily analyzed from the graph in Fig. 3.11. The sensitivity increases with the logarithm of time as shown in Eq. 3.2.

$$S = a \lg(t) + 1 \quad (3.2)$$

where a is a constant that represents the sensitivity change per decade of exposure time and 1 indicates that the resistance measurement is that of the dilution gas when the sensor is not being exposed to the test gas.

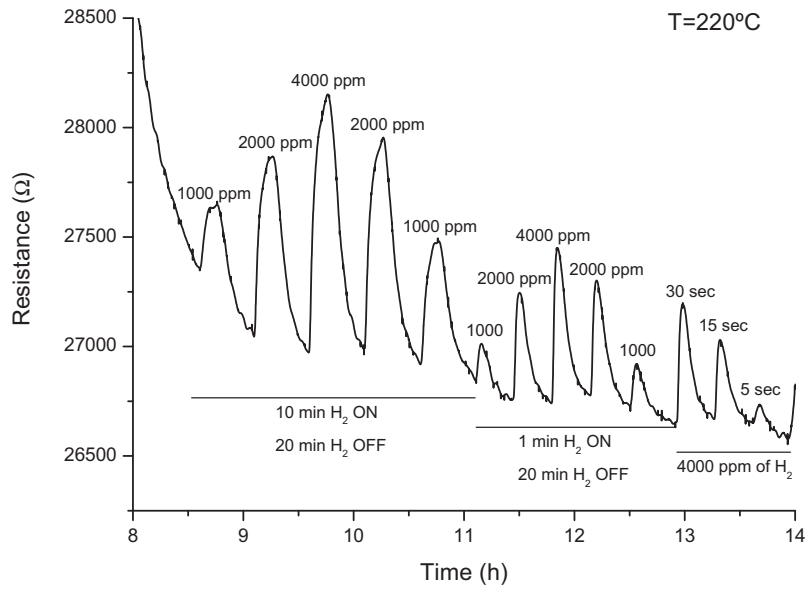


Figure 3.7: Test results at 220°C

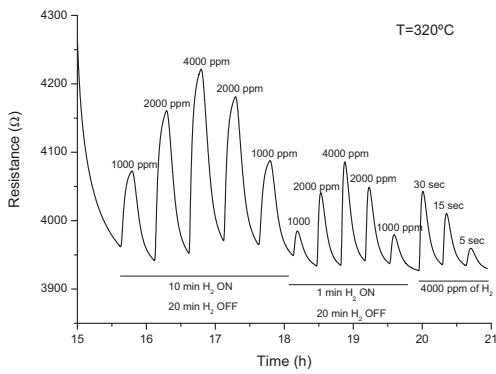


Figure 3.8: Test Results at 320°C

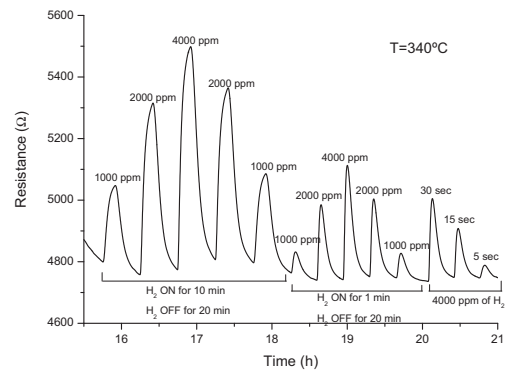


Figure 3.9: Test results at 340°C

Table 3.1: Sensitivity at different exposure times and temperatures for 4000 ppm H₂ gas.

Exposure time (sec)	$S_{200^{\circ}C}$	$S_{220^{\circ}C}$	$S_{320^{\circ}C}$	$S_{340^{\circ}C}$	$S_{360^{\circ}C}$
5		1.004	1.006	1.011	1.015
15	1.005	1.015	1.021	1.036	1.041
30	1.009	1.021	1.030	1.057	1.060
60	1.012	1.031	1.040	1.080	1.085
600	1.019	1.057	1.075	1.161	1.180

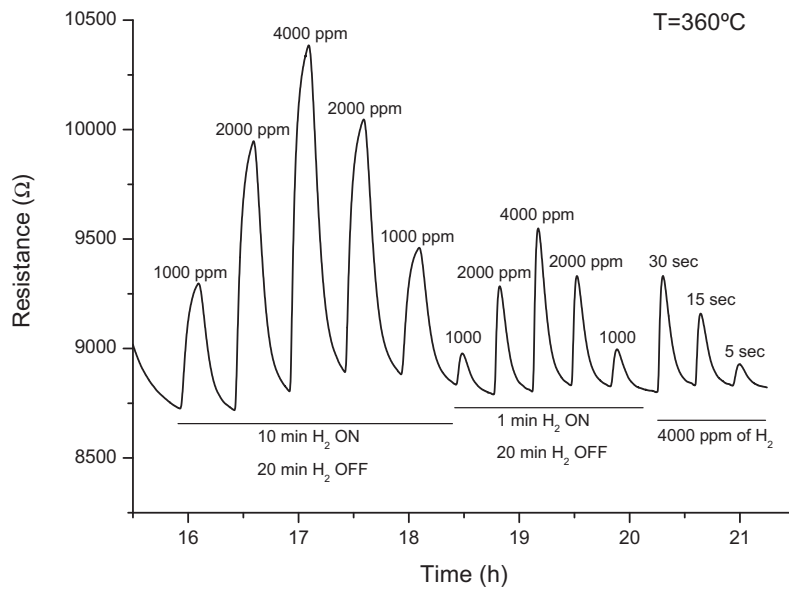


Figure 3.10: Test results at 360°C

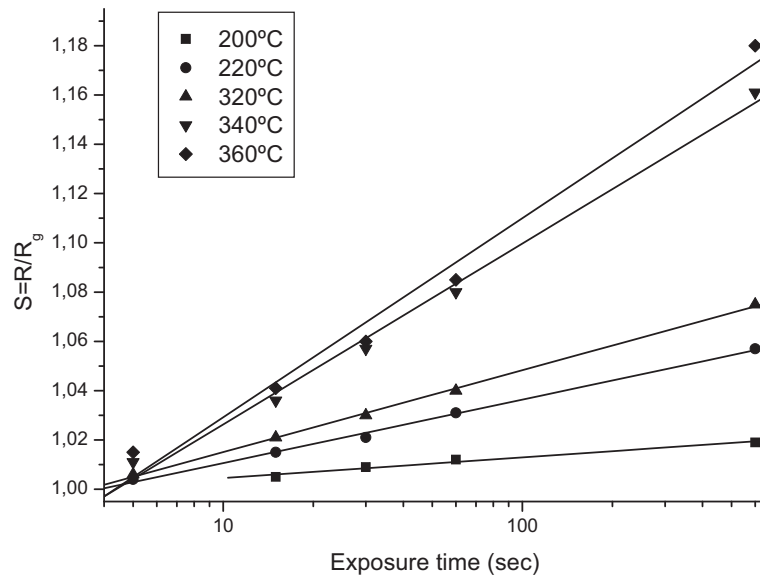


Figure 3.11: Sensor response vs. exposure time for different test temperatures, 4000 ppm of H₂ gas

Eq. 3.2 for each temperature was calculated and results are shown in 3.3-3.7. It can be observed that the slope a , defined before as the sensitivity change per decade of exposure time, increases with increasing testing temperature. This indicates that the sensor response is faster at higher testing temperatures.

$$S_{200^{\circ}C} = 0.0084 \lg(t) + 0.9961 \quad (3.3)$$

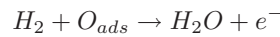
$$S_{220^{\circ}C} = 0.0258 \lg(t) + 0.9849 \quad (3.4)$$

$$S_{320^{\circ}C} = 0.0333 \lg(t) + 0.9818 \quad (3.5)$$

$$S_{340^{\circ}C} = 0.0734 \lg(t) + 0.9528 \quad (3.6)$$

$$S_{360^{\circ}C} = 0.0808 \lg(t) + 0.9484 \quad (3.7)$$

Furthermore, a 50% of the sensitivity change (from $S_0 = 1$ to $S_t = S$) attainable upon 10 minutes of exposure to the analyte occurs in the first minute. This indicates that the mechanism by which hydrogen sensing takes place is a combination of the two explained in Chapter 1. First, a fast linear surface reaction comes about, in which the adsorbed oxygen reacts with hydrogen as indicated in Eq. 1.4 repeated here.



Then, as the surface concentration of adsorbed oxygen diminishes, oxygen from the bulk of the CuO diffuses to the surface and reacts with hydrogen gas. Simultaneously, Cu^{+2} is reduced to Cu^{+1} creating copper vacancies. Now, the reaction is diffusion controlled and therefore, no longer linear. As time passes, deeper oxygen has to diffuse to the surface to react with hydrogen and the reaction slows down. Resistance vs. time graphs show a change in slope which indicates that the reaction slows down after 1 minute of exposure to the target gas. This might prove that oxygen from the bulk diffuses to the surface to react with the analyte. Fig. 3.12 summarizes the explained reaction.

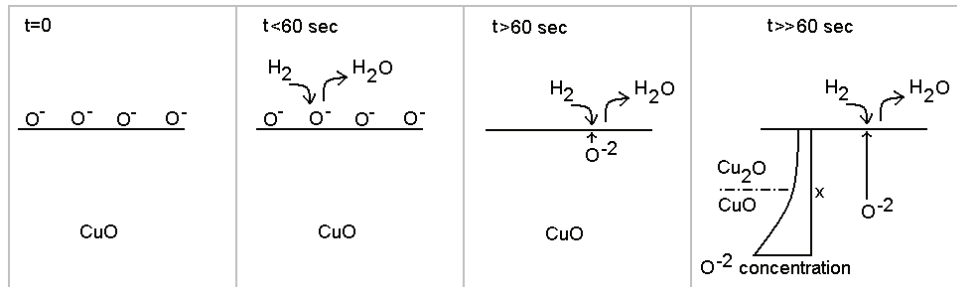


Figure 3.12: Reaction progression and sensing mechanism change.

3.2 Alternative Explanation for the Sensing Mechanism in Terms of Intergranular Potential Barriers

The characterization of the CuO thin film by Scanning Electron Microscopy indicated that the oxide is polycrystalline (see subsection 3.3.2). Therefore, band bending at grain boundaries can be present given that grain size is large enough for a specific acceptor concentration. Band bending refers to the local change in electron bands due to surface charge effects. In the vicinity of grain boundaries, due to intergrain states, bands bend as shown in Fig. 3.13.

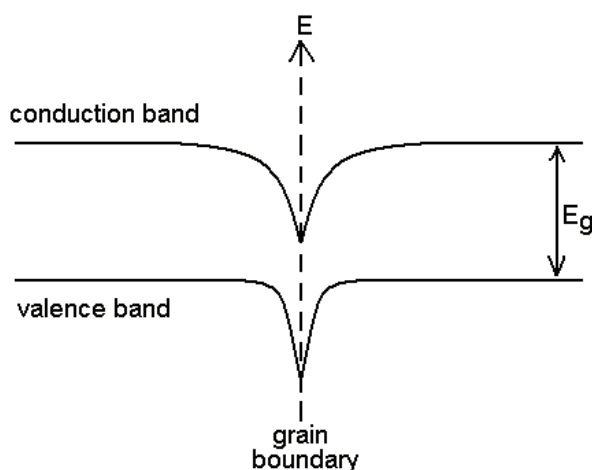


Figure 3.13: Band bending at grain boundaries

The figure shows the potential that corresponds to electrons. However, the majority of the carriers in CuO are “electron holes” located in the valence band. Therefore, the potential for holes is in the opposite direction to the one shown in Fig. 3.13. This can be observed in Fig. 3.14. From this, it can be concluded that the potential bends forming a double parabolic Schottky-type potential barrier.

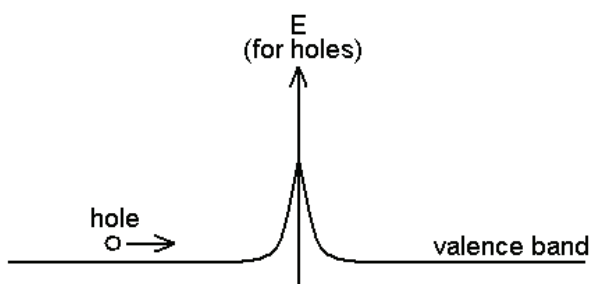


Figure 3.14: Potential corresponding to holes

For conduction from one grain to another to take place, holes have to go through or over the double parabolic potential barrier. There are two possible mechanisms to overcome these potential barriers at grain boundaries. The first one implies that the carriers have to go through the barrier by tunneling. The second

one involves thermionic conduction which takes place when the holes overcome the barrier by “jumping” over it.

In the previous section, it was observed, at low temperatures, that resistance drops when temperature rises and viceversa (see Fig. 3.4). However, at the testing temperatures the expected behavior is the opposite (see Fig. 3.3), i.e. the resistance should slightly increase with temperature. Then, what is wrong?

As it was explained before, conduction takes place either by tunneling or thermionic conduction. Both mechanisms, are favored at higher temperatures. Therefore, holes have more energy to jump over intergrain barriers or tunnel through them when the temperature is increased. Then, the result shown in Fig. 3.4 indicates that the main conduction mechanism is related to inter-granular potential barriers.

When the sensor is exposed to hydrogen gas what happens, in terms of intergrain barriers, is that the bands bend even more and then the barrier becomes higher and wider making it harder for carriers to go through or over it. This is experimentally measured as an increase in the sensor resistance. When the sensor is exposed to the dilution gas (air for this work), the interaction between oxygen and grain surfaces produces the transfer of electrons from the bulk to the surface. From this process, barrier heights diminishes and, as a consequence, the sample resistance decreases for a p-type semiconductor like CuO.

Furthermore, the increase of sensitivity at higher testing temperatures for a given exposure time (see Fig. 3.11) indicates that grain boundary resistance decreases with temperature, effect that is also expected since current transport mechanisms are all thermally facilitated [31].

3.3 Characterization of CuO

3.3.1 X-Ray Diffraction

X-ray diffraction patterns of CuO thin films oxidized in air at 700°C have been widely reported in literature [12], [14], [29]. Therefore, no X-ray diffraction was performed on the thermally oxidized samples used for this work.

3.3.2 Scanning Electron Microscopy

After testing, the sensing material on the micro-chemical sensors was characterized by Scanning Electron Microscopy. In Figs. 3.15 and 3.16 the microstructure of the sensing material can be observed.

The CuO sensing material microstructure is conformed by grains of a wide grain size distribution ranging from 0.1 to 1 μm . The rough and bumpy CuO surface after the oxidation process is due to the volume expansion that occurs during Cu to CuO conversion. The surface of CuO thin films has been reported to become rougher and rougher with the oxidation temperature due to the increasing crystal growth rates [12].

Although the surface appears to be rough containing hills and valleys, the oxide does not show signs of porosity: it is completely dense. Porosity is a crucial characteristic, as explained in Chapter 1, because the greater the surface area the higher sensitivity to the analyte and the shorter the response times. For this reason, current research in the area, and specifically this work (see Chapter 4), suggests that sensing materials in the nanoscale show a better performance.

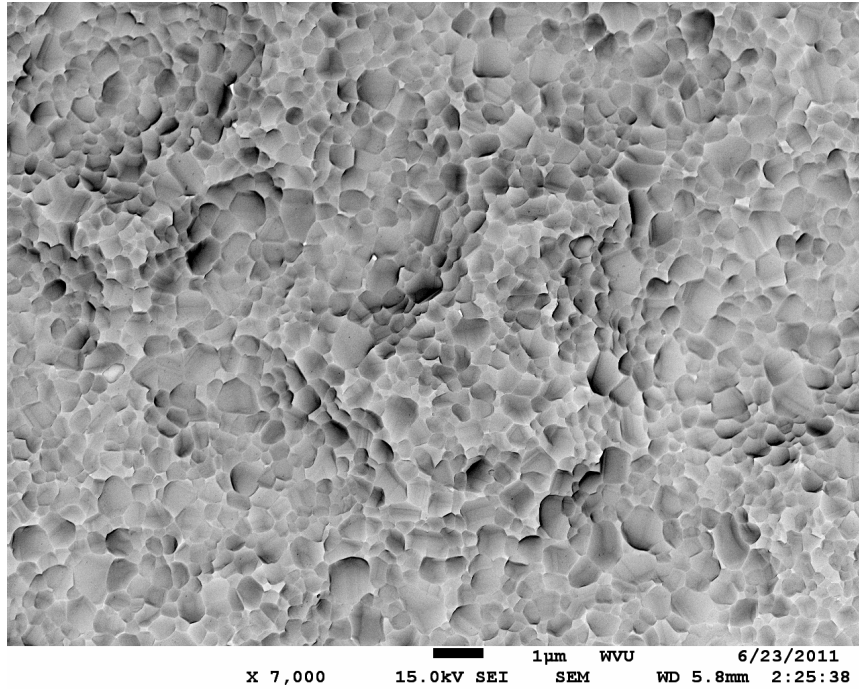


Figure 3.15

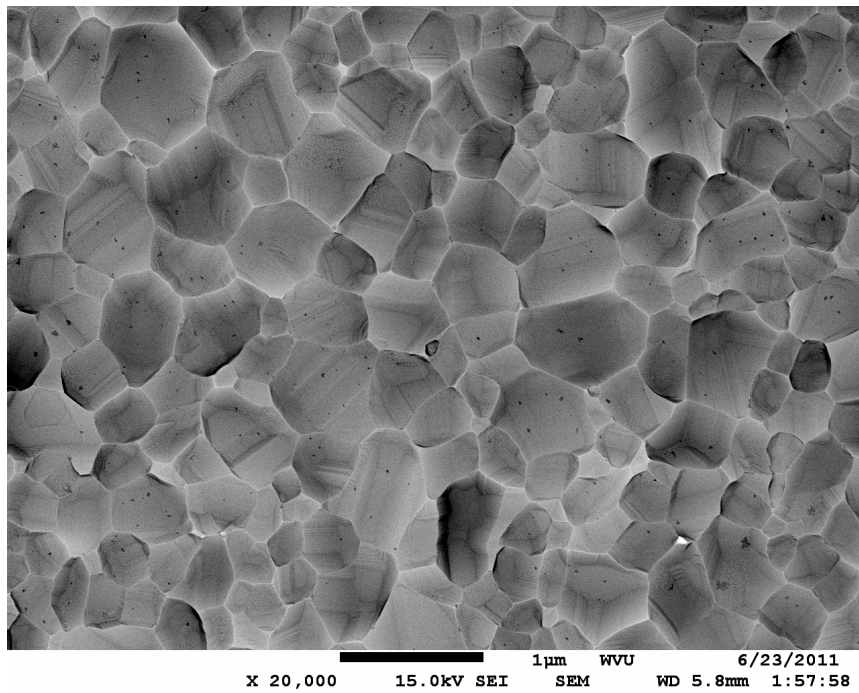


Figure 3.16

In section 2.3.2, it was explained that literature indicates that given a high enough heating rate, high surface to volume ratio CuO nanowires can be obtained. However, no CuO nano-wires were observed in any of the samples. This might be due to a low heating rate or a short dwell time at the highest temperature.

Chapter 4

Results: Route 2, Hydrothermal Process

Although materials in the nano-scale have the disadvantage of suffering solid state reactions at lower temperatures than micro-scale materials, given that their high surface area represents a high driving force to get to the thermodynamically stable state, it is expected to obtain working chemical sensors with increased sensitivity at low testing temperatures. It was previously explained (see Chapter 1) that sensing materials in the nano-scale show enhanced sensitivity. Some of the relevant work done in the area [11] [12] [13], indicate that enhanced sensitivity is the result of higher surface area for gas interaction. However, this can be also explained in terms of electronic bands.

In this Chapter, test results obtained from nano-CuO sensing material produced by a hydrothermal process are analyzed. It is the aim of this Chapter to show results supporting the exposed hypothesis and explain how the sensing mechanism in terms of band bending is altered by the reduction in grain size.

4.1 Test Results

In Figs. 4.1, 4.2 and 4.3 test results are shown. It is observed that at 200°C, the sensor does not stabilize and there is a monotonously increase in resistance. These might be, once again, the result of the sensor interaction with its environment which is thought to involve very large time constants. At higher testing temperatures, 300 and 400°C, the sensor seems to be stable during the extent of the test.

Let's define the change in sensitivity ΔS as the difference between the sensitivity in the dilution gas, $S_g = 1$, and the sensitivity upon exposure to the analyte for a certain time, S .

$$\Delta S = S_g - S = 1 - S \quad (4.1)$$

Table 4.1, shows the sensitivity at different temperatures and exposure times for an analyte concentration of 4000 ppm. By comparing these results with those in Table 3.1 in Chapter 3, it can be concluded that the change in sensitivity in the thermally oxidized samples is as low as 10% of the change in sensitivity in

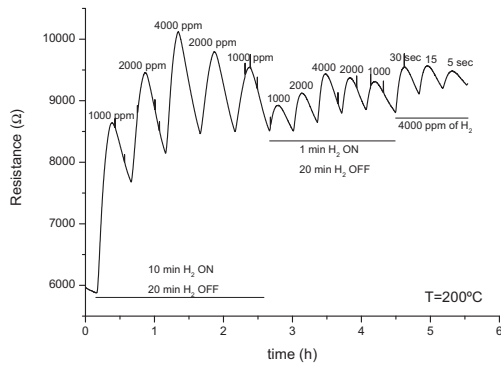


Figure 4.1: Test results at 200°C

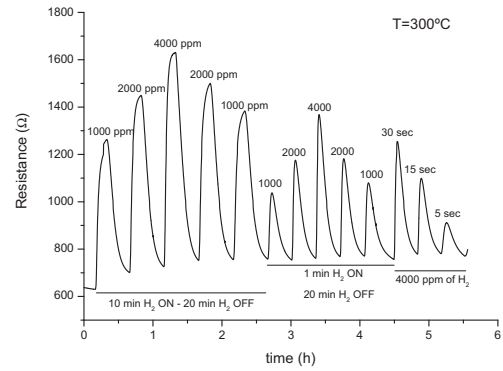


Figure 4.2: Test results at 300°C

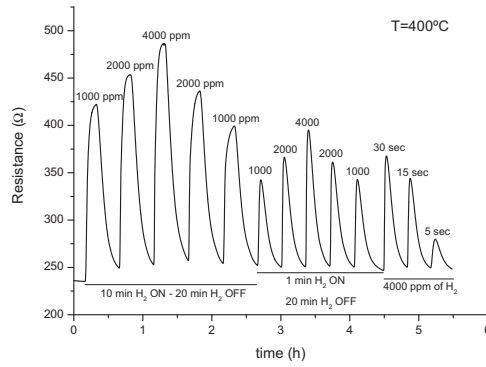


Figure 4.3: Test results at 400°C

the hydrothermally obtained samples. Taking into account that the thermally oxidized samples have a grain size in the order of $1\mu\text{m}$ and the hydrothermally obtained ones are about 25-50nm in width (see Sub-section 4.3.2), it can be reasoned out that the higher the surface area (or smaller the grain size), the higher the sensitivity.

Table 4.1: Sensitivity at different exposure times and temperatures for 4000 ppm H_2 gas.

Exposure time (sec)	$S_{200^\circ\text{C}}$	$S_{300^\circ\text{C}}$	$S_{400^\circ\text{C}}$
5	1.031	1.168	1.121
15	1.049	1.412	1.375
30	1.083	1.660	1.491
60	1.091	1.799	1.578
600	1.242	2.248	1.925

The sensor response was represented against the exposure time for different temperatures given an analyte concentration of 4000 ppm in Fig. 4.4. It can be observed that 50% of the total change in sensitivity attained

in 10 min of exposure to the target gas occurred during the first 30 sec of exposure. After this, the reaction slows down. This may indicate that from $t = 0$ to $t = 30$ sec, hydrogen molecules react with the adsorbed oxygen from the surface. Then, as the surface gets depleted of adsorbed oxygen, the reaction slows down while oxygen from the bulk diffuses to the surface to react with the analyte.

The presence of a diffusion controlled second half of the reaction could also be explained by the long recovery times (around 20 min) given that oxygen from the dilution gas has to adsorb onto the surface and afterwards, diffuse into the nano-crystals.

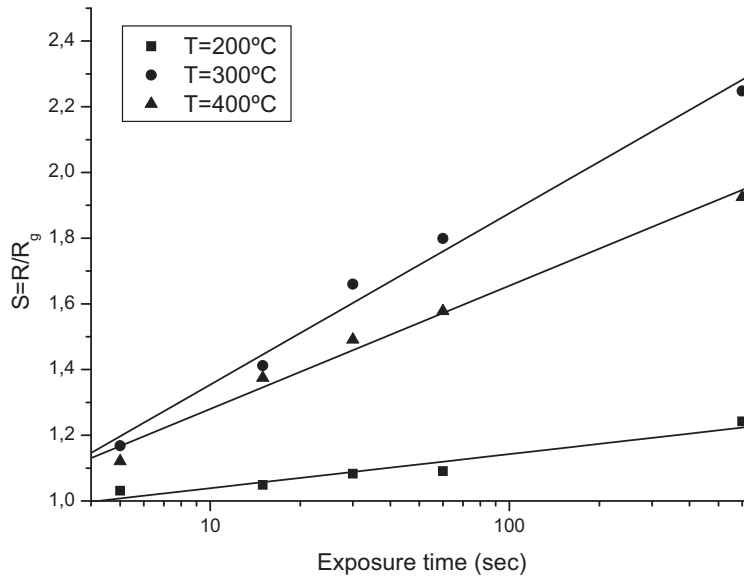


Figure 4.4: Sensor response vs. exposure time for different test temperatures, 4000 ppm of H_2 gas

A remarkable result shown in Fig. 4.4 is that the sensitivity increases when testing temperature increases up to $300^\circ C$ and then diminishes again. Therefore, the highest sensitivity at all times was obtained on samples tested at $300^\circ C$. This can also be observed in Eqs. 4.2-4.4, where a (remember Eq. 3.2) known as the sensitivity change per decade of exposure time is the highest for $300^\circ C$.

$$S_{200^\circ C} = 0.1037 \lg(t) + 0.9351 \quad (4.2)$$

$$S_{300^\circ C} = 0.5220 \lg(t) + 0.8318 \quad (4.3)$$

$$S_{400^\circ C} = 0.3753 \lg(t) + 0.9044 \quad (4.4)$$

A similar result was found in literature [12], where CuO thin film chemical sensors were tested upon exposure to 6% H_2 gas in air at three different operating temperatures: 200, 250 and $300^\circ C$ given the

highest sensitivity at 250°C and the lowest at 200°C.

4.2 Sensing Mechanism in Terms of Intergranular Potential Barriers

4.2.1 Gas Sensing Mechanism and the Role of Surface Reactions

When exposed to air, freshly prepared copper oxide particles adsorb oxygen atoms on the surface, according to



Thus, oxygen atoms pick up electrons when adsorbed on the particle surface as O^- ions. Each CuO particle is covered with negatively charged O^- ions on the surface. On the other hand, due to the depletion of holes, there exists a layer of negatively charged acceptor atoms just below the particle surface. Each CuO particle, thus, has a space-charge layer near its surface, the depth of which primarily depends on the surface coverage of oxygen adsorbates and intrinsic hole concentration in the bulk (depletion layer, L). Other oxygen adsorbates such as O_2^- and O^{2-} are also known to cover the surface of semiconductor metal oxides in air. However, O^- is the most reactive with the inflammable gases within a temperature range of 300-500°C, in which most semiconductors gas sensors are operated [32].

A typical linear arrangement of CuO particles, which may be encountered in a semiconductor gas sensor used in the form of either thin/thick films or pellets, is shown in Fig. 4.5. The presence of an electrical double layer at each grain boundary decreases the potential barrier for the conduction of holes. Hence, a p-type oxide semiconductor exhibits low electrical resistance in air. When the sensor is exposed to an atmosphere containing inflammable gases at elevated temperature, the O^- adsorbates react with the inflammable gases and release the electrons. As a result, the depth of the space-charge layer increases, causing an increase in the height of the potential barrier for the conduction of holes at the grain boundaries. The overall resistance of the sensor raises and its electrical conductivity decreases. The sensitivity of the gas sensor is then determined as the ratio of its resistance in air to that in a sample gas containing inflammable components [33].

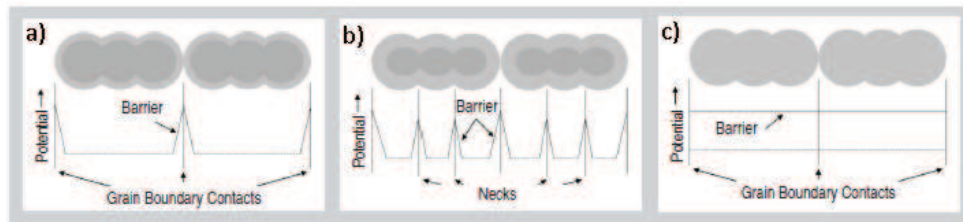


Figure 4.5: A model of the variation in potential barrier to electronic conduction with respect to changes in the crystallite size. a) $D \gg 2L$, b) $D \geq 2L$, c) $D < 2L$, where D is the crystallite size and L is the space-charge layer thickness. In a-c, the potential barrier is mainly controlled by the grain-boundaries, the necks, and the grains, respectively. *Reproduced from [33]*

4.2.2 Effect of Particle Size on Sensitivity

A semiconductor gas sensor has two functions. The receptor function (i.e., surface oxygen) recognizes or identifies a chemical gas component. If a metal or a metal oxide is added onto the surface as a surface modifier, it may influence the receptor function. The transducer function transforms the chemical signal into an electrical signal. In this case, the holes generated via chemical reaction are conducted through the material. As these conduction of holes have to overcome the potential barrier induced by the space-charge layer, the microstructure of these sensors plays the key role in controlling the transducer function. The magnitude of this potential barrier to electronic conduction strongly depends on the ratio of the crystallite size D to the space-charge layer thickness L [32].

In a semiconductor gas sensor, the crystallites are connected to each other via necks forming aggregates (i.e., large particles). The large particles are, in turn, connected to the neighbors via grain boundary contacts. When the crystallite size is very large $D \gg 2L$, the conduction holes have to overcome the potential barrier induced by the space-charge layer at each grain boundary contact (Fig. 4.5 a). In this situation, the resistance of the gas sensor is determined by the resistance offered by the grain boundary contacts, which is independent of the grain size. Hence, when the crystallite size is very large compared to the space-charge layer $D \gg 2L$, the sensitivity of an oxide semiconductor is independent of the crystallite size.

As the crystallite size decreases, the space-charge layer penetrates deeper into each of the crystallites. When the crystallite size approaches the space-charge layer thickness $D \geq 2L$, the space-charge layer forms channels at each neck within a particle (Fig. 4.5 b). As the conduction holes must move through these channels, they experience potential barriers in addition to the potential barrier existing at the grain boundary. Under these constraints, the resistance of the gas sensor is determined predominantly by the neck resistance. As the neck size is observed to be proportional to the crystallite size, the sensitivity of the gas sensor is dependent on the crystallite size when $D \geq 2L$.

As the crystallite size reduces below two times the space-charge layer thickness $D < 2L$, the entire crystallite becomes depleted of carriers. The space-charge layer then penetrates into the crystallite completely (Fig. 4.5 c). The electrical resistance of the gas sensor decreases abruptly and is controlled mainly by the grain resistance [33]. In this region, given that the ratio between surface area and volume increases abruptly ($S/V \uparrow$), the number of carriers also increases for a specific oxygen gas partial pressure. The sensors sensitivity is high and conduction is accurately explained by means of bulk conduction mechanisms.

4.3 Characterization of the nano-crystals obtained by the hydrothermal process

4.3.1 X-Ray Diffraction

Cu_2O can be identified by its peaks at $2\theta = 29.5^\circ$, 36.4° (\dagger), 42.3° (\ddagger), 61.6° , 73.8° and 77.6° . These correspond to (110), (111), (200), (220), (311) and (222) [34]. CuO can be identified by its most relevant peaks located at $2\theta = 32.5^\circ$, 35.6° (\dagger), 38.8° (\ddagger), 48.7° , 53.4° , 58.3° , 61.6° , 66.5° , 68.2° , 72.4° and 75.3° . These peaks are indexed to CuO (110), (111), (111), (202), (020), (202), (113), (310), (220), (311) and (222) [13]. \dagger corresponds to the highest peak and \ddagger corresponds to the second highest peak.

The remaining solution from the hydrothermal process called Run 1 was dried and the powder obtained was used for XRD characterization. The XRD graph obtained is presented in Fig. 4.6. It can be seen that the peaks corresponding to CuO are present in the sample.

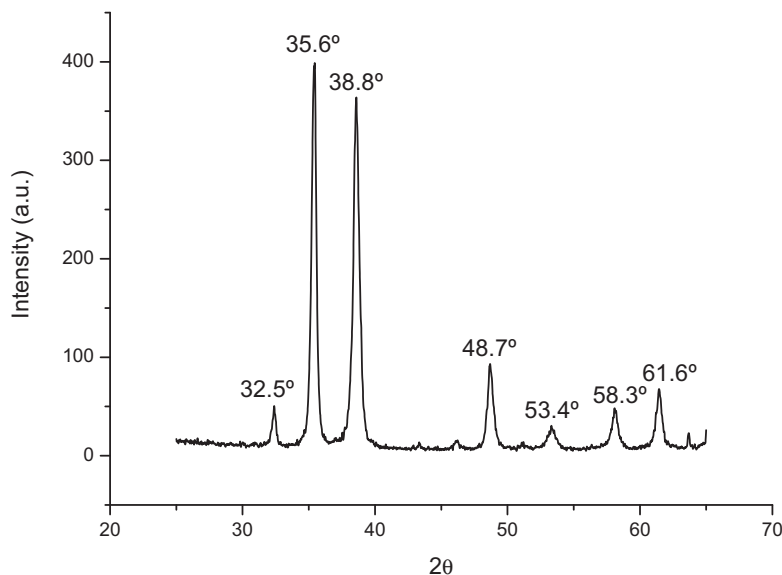


Figure 4.6: XRD results for powder obtained from solution Run 1

4.3.2 Scanning Electron Microscopy

The nano-crystals grown onto the Cu seed using the three solutions, called “Run 1, 2 and 3”, described in Table 2.2 (see Chapter 2) in a hydrothermal process were characterized by Scanning Electron Microscopy.

In Figs. 4.7 and 4.8 the results from the hydrothermal process using solution “Run 1” are presented. The copper oxide nano-crystals cover the whole surface previously seeded with Cu. When using higher magnifications, platelets with thicknesses in the nano-scale can be observed. From these images, it can be concluded that the sensing material has a very high surface area. This property is desired for sensing purposes, since higher surface area implies higher sensitivity. As described in Chapter 1, non-equilibrium surfaces enhance gas adsorption, i.e., an ultra high surface area facilitates gas interaction.

Results obtained from “Runs 2 and 3” are presented in Figs. 4.9 and 4.10. In these images, it can be seen that the copper oxide particles do not cover the entire surface of Cu seeds. Instead, they form isolated spheres. Higher magnifications show that the spheres are formed by platelets with similar dimensions to those of Fig. 4.8. Nevertheless, the results from these runs are undesirable since the CuO crystals are not creating a bridge between the fingers of the IDEs. Therefore, the sensor is not conductive and cannot serve its purpose. These results might indicate solution saturation for high concentrations of $\text{Cu}(\text{NO}_3)_2$ in de-ionized water.

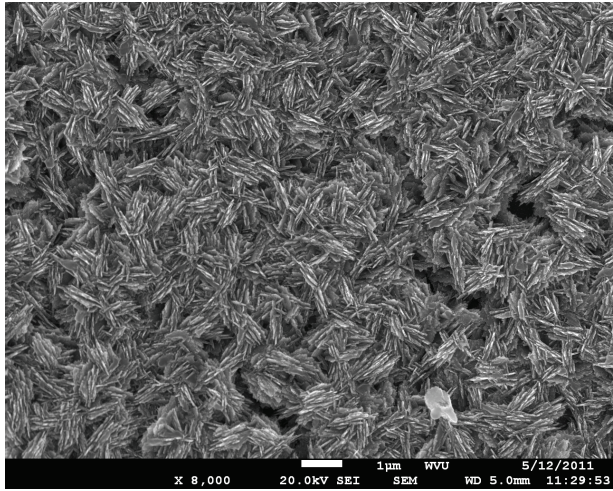


Figure 4.7: SEM results of solution Run 1 - x8000

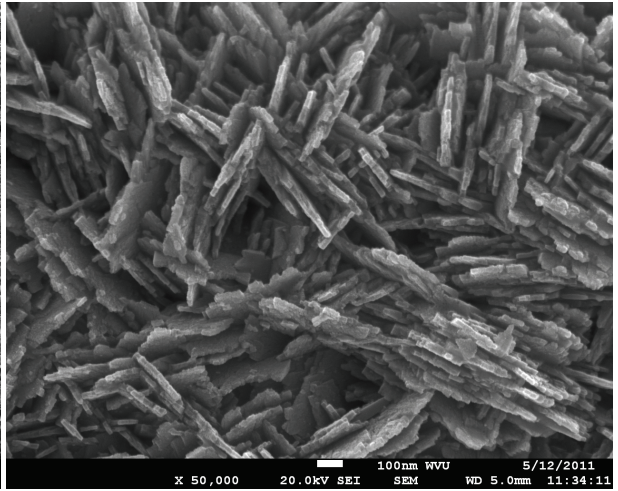


Figure 4.8: SEM results of solution Run 1 - x50000

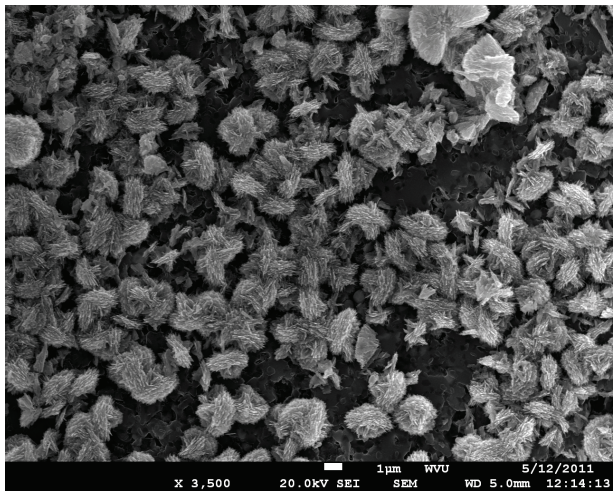


Figure 4.9: SEM results of solution Run 2 - x3500

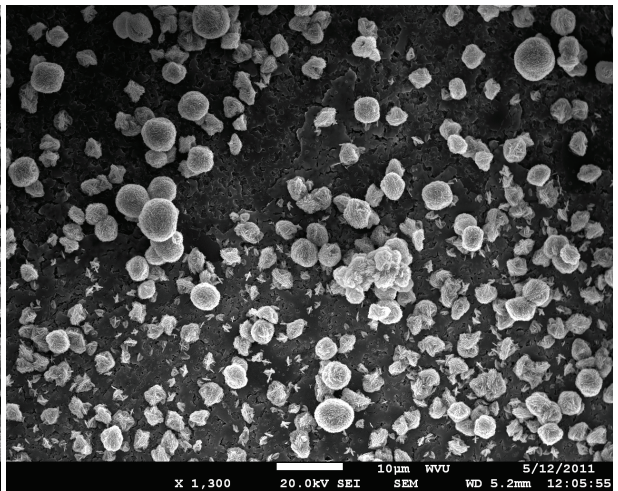


Figure 4.10: SEM results of solution Run 3 - x1300

In all three cases, the platelets have the thickness dimension in the nano-scale ranging from 25 to 50 nm and they seem to grow perpendicular to the surface.

Chapter 5

Conclusions

Nano-derived CuO micro-chemical sensors were successfully developed and tested upon exposure to hydrogen gas. The sensing material was obtained with two different processing routes which led to different morphologies. Results indicated that the performance is enhanced when the grain size of the sensing material is reduced in agreement with theoretical predictions.

During the extent of this work, it was proven that cupric oxide is sensitive to hydrogen gas in a variety of concentrations, ranging from 1000-4000 ppm. Although these concentrations may be high compared to those encountered while dealing with explosive materials, results obtained in the present work represent a step forward to meeting the objective of remotely detecting them. In addition, these sensors may have application in industrial processes where higher hydrogen concentrations have to be detected to ensure process control and safety management.

As it was predicted by literature [11] [24], it was confirmed that the sensitivity S increases linearly with H_2 concentration. It was also observed that the response increases linearly with the logarithm of exposure time, which indicated that the resistance changes more abruptly during the first minute of exposure (thermally oxidized CuO) or within 30 seconds of exposure (hydrothermally obtained CuO). As these can be considered the response times for both kinds of sensors, it can be concluded that the smaller the grain size, the faster the response time.

A fast response time has been described as one of the most important characteristics of metal-oxide sensors. In the present work, thermally oxidized CuO and hydrothermally obtained CuO as well responded to hydrogen presence within 5 seconds of exposure to the analyte reassuring fast response. Recovery times, however, have to be improved.

Gas sensing measurements indicated that the sensitivity increases when grain size decreases, $S \uparrow$ as $D \downarrow$. This was explained in terms of inter-granular potential barriers, given that a decrease in grain size would overlap space-charge regions, also known as depletion regions, making potential barriers at grain boundaries disappear, which in turn would make the resistance to be bulk controlled. Data obtained from this work was combined with data from literature [12], and it is presented in Fig. 5.1 where the sensitivity vs. grain size is shown. From this, it can be presumed that sensing materials with grain sizes smaller than 25 nm will have the greatest sensitivity.

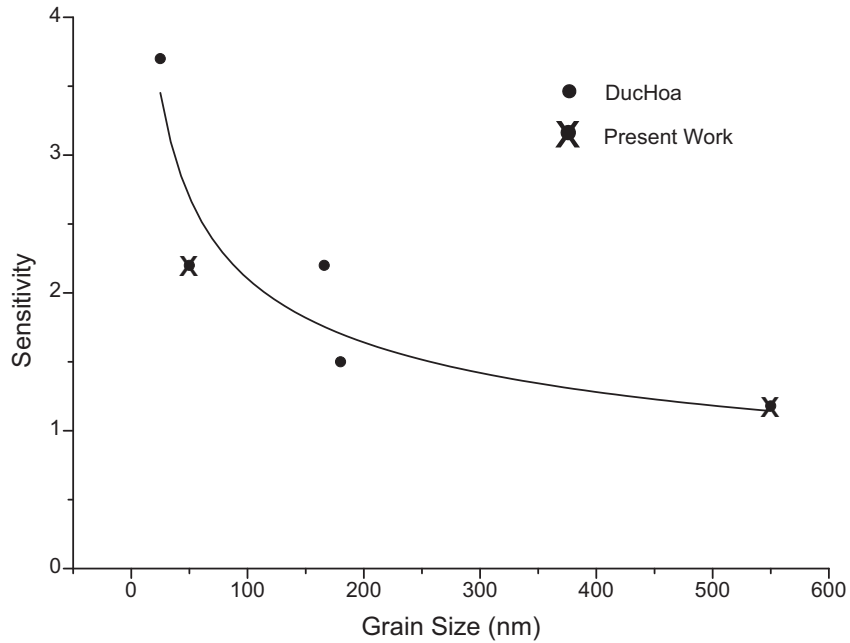


Figure 5.1: Sensor response vs. grain size. • correspond to [12] where CuO sensors were tested at 250°C in 6% H₂ gas. × corresponds to results obtained in the present work. Grain size for hydrothermally obtained CuO was considered to be 50 nm, while the mean grain size for thermally oxidized CuO, 550 nm, was used.

5.1 Future Work

- Test these sensors in other fingerprint gases, such as CO_x, NO_x, SO_x, etc. Analyze their response.
- Produce CuO and modify its surface with noble metals or oxides to increase the sensitivity of the sensors. Noble metals such as Pt are expected to act as a catalyst for catalytic decomposition of inflammable gases over the CuO particle surface, and thus, enhance the spillover of inflammable gases over the CuO particle surface so that they react with the oxygen adsorbate more easily [33]. Some oxides may increase the space charge region making it easier to obtain greater sensitivities.
- Design the best sensor array, in which each sensor has enhanced detection of a singular fingerprint gas, and build a neural network to process data and estimate the explosive that is being detected.

Appendix A

Deposition Rate Studies

A.1 Pt Deposition Rate Study

A deposition rate study was performed using the CVC 610 DC Magnetron sputter station prior to making the electrodes for the sensors.

Pieces of cleaned silicon wafers were used as substrates. A piece of copper tape was used to attach the wafers to the sputter station's substrate holder as shown in Fig. A.1. Pt was sputtered onto the p-type Si wafers for different periods of time. When the sputtering was done, the copper tape was removed, creating a "step" (see Fig. A.2). Measurements of the height of this step were done by means of a profilometer.

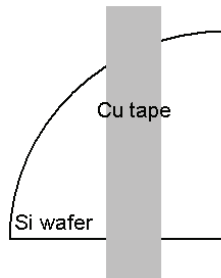


Figure A.1



Figure A.2

Results to this study can be seen in Fig. A.3. The average values of the measurements for each time were used to calculate the deposition rate (See Fig. A.4). From this graph, the deposition rate for Pt can be calculated as 56.6 nm/min.

A.2 Cu Deposition Rate Study

Using the same procedure as for the *Pt Deposition Rate Study*, the deposition rate of Cu was obtained. Measurements done for this study are shown in Fig. A.5. Average measurement results are represented in Fig. A.6. Cu deposition rate: 67.9 nm/min.

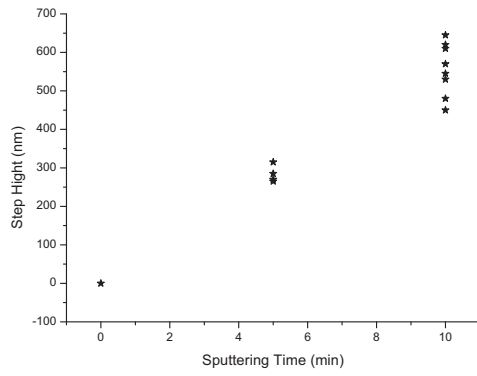


Figure A.3: Pt step height profilometer measurements

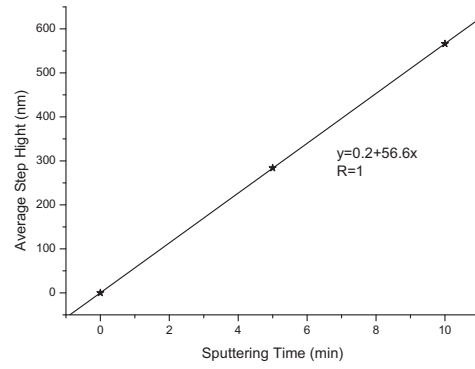


Figure A.4: Average values of Pt step height

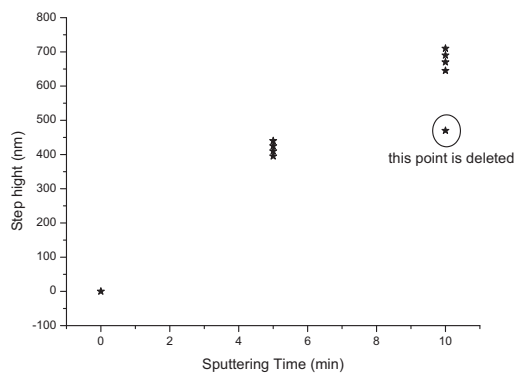


Figure A.5: Cu step height profilometer measurements

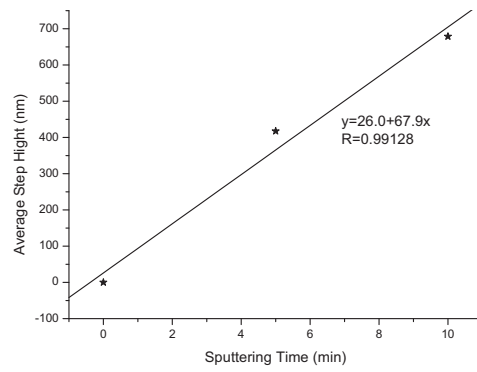


Figure A.6: Average values of Cu step height

Appendix B

Inter-Digitated Electrodes Dimensions

In Fig. B.1, the schematics of the Pt electrodes made during this work is shown. Dimension of the electrode can be seen on Table B.1. From this, the area of the Cu rectangles can be calculated as

$$A_{Cu} \simeq (c - 2a)b = 3.734 \text{ mm}^2$$

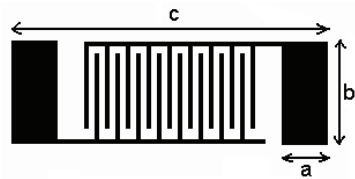


Figure B.1: Pt IDEs dimensions

Table B.1: Dimensions of Pt electrode.

	(μm)
a	750
b	1150
c	4747.31

The copper sputtering time was 8 minutes. Using the results from Appendix A, the copper thickness can be calculated to be 500 nm.

Bibliography

- [1] J. Yinon. Detection of explosives by electronic noses. *Anal. Chem. A*, 75:98A–105A, 2003.
- [2] Y. Gui, C. Xie, J. Xu and G. Wang. Detection and discrimination of low concentration explosives using MOS nanoparticle sensors. *Journal of Hazardous Materials*, 164, 2009.
- [3] S. Content, W. C. Trogler and M. J. Sailor. Detection of nitrobenzene, DNT and TNT vapors by quenching of porous silicon photoluminescence. *Chem. Eur. J.*, 6:2205–2213, 2000.
- [4] American Friends of Tel Aviv University. Out-sniffing bomb-sniffing dog. *Science Daily*, 2010.
- [5] M. Niper, Y. Quian, R. Scott Carr and K. Miller. Degradation of picric acid and 2,6-DNT in marine sediments and water: the role of microbial activity and UV exposure. *Chemosphere*, 56:519–530, 2004.
- [6] M. R. Darrach, A. Chutjian and G. A. Plett. Trace explosive signatures from WWII unexploded undersea ordnance. *Environ. Sci. Technol.*, 32:1354–1358, 1998.
- [7] B. L. Zhu, C. S. Xie, W. Y. Wang, K. J. Huang and J. H. Hu. Improvement in gas sensitivity of ZnO thick films of volatile organic compounds (VOCs) by adding TiO₂. *Mater. Lett.*, 58:624–629, 2004.
- [8] M. Garcia, M. Aleixandre, J. Gutierrez and M. C. Horrillo. Electronic nose for wine discrimination. *Sens. Actuators B*, 113:911–916, 2006.
- [9] Q. Y. Zhang, C. S. Xie, S. P. Zhang, A. H. Wang, B. L. Zhu, L. Wang and Z. B. Yang. Identification and pattern recognition analysis of chinese liquors by doped nano ZnO gas sensor array. *Sens. Actuators B*, 110:370–376, 2005.
- [10] T. Hübner, L. Boon-Brett, G. Black and U. Banach. Hydrogen sensors - A review. *Sens. Actuators B*, 2011.
- [11] D. Barreca, E. Comini, A. Gasparotto, c. Maccato, C. Sada, G. Sberveglieri and E. Tondello. Chemical vapor deposition of copper oxide films and entangled quasi-1D nanoarchitectures as innovative gas sensors. *Sens. Actuators B*, 141:270–275, 2009.
- [12] N. Duc Hoa, S. Y. An, N. Q. Dung, N. V. Quy and D. Kim. Synthesis of p-type semiconducting cupric oxide thin films and their application to hydrogen detection. *Sens. Actuators B*, 146:239–244, 2010.
- [13] H. T. Hsueh, T. J. Hsueh, S. J. Chang, F. Y. Hung, T. Y. Tsai, W. Y. Weng, C. L. Hsu and B. T. Dai. CuO nanowire-based humidity sensors prepared on glass substrate. *Sens. Actuators B*, 2011.

- [14] J. Liang, N. Kishi, T. Soga and T. Jimbo. Cross-sectional characterization of cupric oxide nanowires grown by thermal oxidation of copper foils. *Applied Surface Science*, 257:62–66, 2010.
- [15] A. A. Ogwu, T. H. Darma and E. Bouquerel. Electrical resistivity of copper oxide thin films prepared by reactive magnetron sputtering. *Journal of Achievements in Materials and Manufacturing Engineering*, 24:172–177, 2007.
- [16] L. Wang. Preparation and characterization of properties of electrodeposited copper oxide films. *Ph. D Thesis - Univ. of Texas at Arlington*, page 17, 2006.
- [17] J. Pike, S.W. Chan, F. Zhang, X. Wang and J. Hanson. Formation of stable Cu_2O from reduction of CuO nanoparticles. *Applied Catalysis A: General*, 303:273–277, 2006.
- [18] D. Kohl. Function and application of gas sensors. *J. Phys. D: Appl. Phys.*, 34:R125–R149, 2001.
- [19] N. Barsan and U. Weimar. Conduction model of metal oxide gas sensors. *J. Electroceram.*, 7:143–167, 2001.
- [20] V. I. Gaman. Basic physics of semiconductor hydrogen sensors. *Russ. Phys. J.*, 51:425–441, 2008.
- [21] J. Zhang, J. Liu, Q. Peng, X. Wang and Y. Li. Nearly monodisperse Cu_2O and CuO nanospheres: Preparation and applications for sensitive gas sensors. *Chem. Mater.*, 18:867–871, 2006.
- [22] X. Gou, G. Wang, J. Yang, J. Park and D. Wexler. Chemical synthesis, characterization and gas sensing performance of copper oxide nanoribbons. *J. Mater. Chem.*, 18:965–969, 2008.
- [23] X. Wang, X. Q. Fu, X. Y. Xue, Y. G. Wang and T. H. Wang. Surface accumulation conduction controlled sensing characteristics of p-type CuO nanorods induced by oxygen adsorption. *Nanotechnology*, 18:145506/1–145506/5, 2007.
- [24] Y. Zhang, X. He, J. Li, H. Zhang and X. Gao. Gas-sensing properties of hollow and hierarchical copper oxide microspheres. *Sens. Actuators B*, 128:293–298, 2007.
- [25] Y. S. Kim, I. S. Hwang, S. J. Kim, C. Y. Lee and J. H. Lee. CuO nanowire gas sensors for air quality control in automotive cabin. *Sens. Actuators B*, 135:298–303, 2008.
- [26] S. T. Shishiyanu, T. S. Shishiyanu and O. I. Lupan. Novel NO_2 gas sensor based on cuprous oxide thin films. *Sens. Actuators B*, 113:468–476, 2006.
- [27] J. Tamaki, K. Shimano, Y. Yamada, Y. Yamamoto, N. Miura and N. Yamazoe. Dilute hydrogen sulfide sensing properties of CuO-SnO_2 thin film prepared by low-pressure evaporation method. *Sens. Actuators B*, 49:121–125, 1998.
- [28] M. Kaur, K. P. Muthe, S. K. Deshpande, S. Choudhury, J. B. Singh, N. Verma, S. K. Gupta and J. V. Yakhmi. Growth and branching of CuO nanowires by thermal oxidation of copper. *Journal of Crystal Growth*, 289:670–675, 2006.

- [29] J. T. Chen, F. Zhang, J. Wang, G. A. Zhang, B. B. Miao, X. Y. Fan, D. Yan and P. X. Yan. CuO nanowires synthesized by thermal oxidation route. *Journal of Alloys and Compounds*, 454:268–273, 2008.
- [30] L. Solymar and d. Walsh. *Electrical Properties of Materials*. Oxford University Press, 2010.
- [31] C. Malagu, M.C. Carotta, A. Giberti, V. Guidi, G. Martinelli, M.A. Ponce, M.S. Castro and C.M. Aldao. Two mechanisms of conduction in polycrystalline SnO₂. *Sens. Actuators B*, 136:230–234, 2009.
- [32] A. Dutta, D. Das, M.L. Grilli, E. Di Bartolomeo, E. Traversa and D. Chakravorty. Preparation of sol-gel nano-composites containing copper oxide and their gas sensing properties. *Journal of Sol-Gel Science and Technology*, 26:1085–1089, 2003.
- [33] S. Seal and S. Shukla. Nanocrystalline SnO gas sensors in view of surface reactions and modifications. *JOM*, pages 35–38,60, 2002.
- [34] Y. T. Chen, W. Zhang, B. Z. Zhou, X. Q. Xu, Y. Q. Fan, Y. J. Guo and Z. X. Zhang. Polyol process to large-scale synthesis of Cu₂O with disk-like structure. *Chinese Chemical Letters*, 16(2):245–248, 2005.